Vacancy-induced pseudogap formation in antiferromagnetic $Cr_{0.86}ZnSb$

Michael Parzer, Fabian Garmroudi, Herwig Michor, Xinlin Yan, Ernst Bauer, Gerda Rogl, Jiri Bursik, Stephen Cottrell, Raimund Podloucky, and Peter Rogl

Published version information

Citation: Michael Parzer et al., Vacancy-induced pseudogap formation in antiferromagnetic $Cr_{0.86}ZnSb$, Phys. Rev. B 110, 195124

DOI: https://doi.org/10.1103/PhysRevB.110.195124

Vacancy-induced pseudogap formation in antiferromagnetic $Cr_{0.86}ZnSb$

Michael Parzer,[1,*] Fabian Garmroudi,[1] Herwig Michor,[1] Xinlin Yan,[1] Ernst Bauer,[1] Gerda Rogl,[2] Jiri Bursik,[3] Stephen Cottrell,[4] Raimund Podloucky,[2] and Peter Rogl[2]

[1]*Institute of Solid State Physics, TU Wien, Wiedner Hauptstraße 8–10, A-1040 Wien, Austria*

[2]*Institute of Materials Chemistry, Universität Wien, Währinger Straße 42, A-1090 Wien, Austria*

[3]*Institute of Physics of Materials, Czech Academy of Sciences, Žižkova 22, 61662 Brno, Czech Republic*

[4]*ISIS Facility, Rutherford Appleton Laboratory, Chilton, Didcot Oxon OX11 0QX, United Kingdom*

(Received 27 May 2024; revised 23 September 2024; accepted 25 September 2024; published 8 November 2024)

Structural defects are important for both solid-state chemistry and physics, as they can have a significant impact on chemical stability and physical properties. Here, we identify a vacancy-induced pseudogap formation in antiferromagnetic $Cr_{0.86}ZnSb$. $Cr_{1-x}ZnSb$ alloys were studied combining efforts of density functional theory (DFT) calculations and experimental methods to elucidate the effect of vacancies. Detailed analyses (x-ray powder and single-crystal diffraction, transmission and secondary scanning electron microscopy) of $Cr_{1-x}ZnSb$, $0 < x < 0.20$, prompts $Cr_{0.86}ZnSb$ as the only stable compound, crystallizing with the MnAlGe-type structure. From DFT calculations, an antiferromagnetic spin configuration of Cr local magnetic moments was found to be favorable for both the perfectly stoichiometric compound CrZnSb as well as for $Cr_{0.875}ZnSb$. Magnetic order is observed experimentally for $Cr_{0.86}ZnSb$ by temperature- and field-dependent magnetization measurements, revealing a magnetic phase transition near 220 K, which is corroborated by zero-field muon spin relaxation studies. Thermoelectric transport properties exhibit distinct maxima in the temperature-dependent Seebeck coefficient and electrical resistivity at around 190 K. Analyzing the measured data on the basis of a triple parabolic band model and DFT simulations, their characteristic features are traced back to a pseudogap in the electronic structure arising from a particular vacancy arrangement. These findings offer valuable insights into the role of vacancies in defect materials, contributing to the broader understanding of structural defects and their impact on the electronic structure.

DOI: 10.1103/PhysRevB.110.195124

I. INTRODUCTION

Structural defects, particularly vacancies, are known to profoundly influence the macroscopic physical properties of materials, a phenomenon that has been extensively studied in half-Heusler compounds [1–3]. In the field of thermoelectrics, vacancies have been reported to enhance transport properties in specific cases [4–6]. Therefore, a profound understanding of the role of structural defects in these materials is essential for the effective tuning of their electronic properties [7–9]. Moreover, vacancies in half-Heusler structures have been shown to induce long-range magnetic order, similar to the effects observed in oxides [2,10,11].

Half-Heusler alloys are a relevant group of thermoelectric (TE) materials with a promising figure of merit ZT and they have drawn attention due to the discovery of a band gap in {Ti,Zr,Hf}NiSn compounds and impurity states within the gap [12–14]. Record values of the thermoelectric figure of merit were revealed for Sb-doped $Ti_{0.5}Zr_{0.25}Hf_{0.25}NiSn$ which reaches $ZT_{max} \sim 1.5$ [15,16]. Interestingly, the 3*d*-metal series forms *T*ZnSb compounds with different structures depending on the transition metal *T*. For more electropositive elements $T =$ Ti, V, Cr, Mn, Fe, the compounds typically adopt the MnAlGe-type structure. For transition metals with nearly filled 3*d* shells, including Fe at higher temperatures, the compounds crystallize in the half-Heusler-type structure (FeZnSb [17,18], NiZnSb [19]) or form a $2 \times 2 \times 2$ superstructure of the half-Heusler unit cell ($T =$ Fe, Co, $Ru_9Zn_7Sb_8$ type [20]). Quite recently Bensen *et al.* [21] reported on disordered $V_{1-x}ZnSb_{1-y}$ ($x \sim 0.1$, $y \sim 0.05$), for which itinerant charge carriers were said to coexist with a small, localized magnetic moment of around 0.25 μB from the ordered part of the vanadium lattice (MnAlGe type). In a follow-up paper, structural and thermodynamic properties as well as resistivity were reported for *X*ZnSb phases with $X =$ Cr, Mn, Fe, Ni for which sizable amounts of vacancies on transition-metal sites were revealed [22].

Given the intriguing physical properties of $Cr_{1-x}ZnSb$, including a resistivity maximum near room temperature and unresolved magnetic ordering [22], we aim to scrutinize the structure-property relationship in this system, with a particular focus on how the Cr vacancies influence these properties. To analyze transport and magnetic properties using density functional theory (DFT) calculations, experimental results from phase-pure samples must be compared with respect to appropriate supercell calculations.

Accordingly, we focus our investigations on several tasks: (i) to synthesize single-phase $Cr_{1-x}ZnSb$, (ii) to elucidate the crystal structure and defect sites, (iii) to reveal physical properties, including thermal stability, specific heat, electrical conductivity, Seebeck coefficient, and magnetic behavior, and

*Contact author: michael.parzer@tuwien.ac.at

(iv) by elaborate DFT calculations to provide detailed information about the effect of the vacancies on structural stability, magnetic ordering, and magnetic moments, on electronic structure and bonding, and on electronic transport properties.

II. METHODS

A. Experimental techniques

Due to the rather high vapor pressures of Zn and Sb at elevated temperatures, arc melting was avoided and several samples $Cr_{1-x}ZnSb$ ($x = 0$, 0.05, 0.1, 0.14, 0.15, 0.2) were prepared via conventional powder metallurgical sinter techniques from powders of 99.9 mass% Cr (<200 mesh; Alfa Ventron), filings of a 99.8 mass% pure Zn-rod (Alfa Ventron), and freshly powdered 99.99 Sb rod (in a WC-Co mortar) from Alfa Ventron, Germany. The powder blends were compacted without lubricants in a steel die and sealed in a quartz tube. Low thermal stability demanded individual reaction temperatures and, therefore, proper annealing temperatures were extracted from DTA: $Cr_{1-x}ZnSb$ proved to be stable only below <660° C; thus samples were annealed at 550° C. After each second day (for five times) the sinter cake was powdered (< 60 μm), recompacted, and sealed for annealing again. With this procedure rather single-phase products (3–5 g) could be obtained. As in all cases the sinter cake appeared porous, densification was achieved (relative density about 90%) for cylindrical plates (diameter 10 mm, height ∼1 mm) via high-pressure torsion (HPT) at room temperature in steel dies at 4 GPa and up to five revolutions. The measured density, d_A, was derived from Archimedes' principle on the HPT-discs in distilled water. The x-ray density $d_X = MZ/VL$ was calculated from Z as the number of formula units within the unit cell, M as the molar mass in g/mol, V as the volume, and L as Loschmidt's number; the relative density, d_{rel}, was calculated from $d_{rel} = (d_A/d_X) \times 100$.

Polycrystalline powders were analyzed by x-ray powder diffraction with Ge-monochromated Cu $K\alpha_1$ radiation ($\lambda = 0.154056$ nm) employing a Guinier-Huber image plate recording system. Rietveld refinements were performed using the program FULLPROF [23], while precise lattice parameters were obtained from least-squares fits with the program STRUKTUR [24]; Ge served as an internal standard ($a_{Ge} = 0.5657906$ nm).

The analysis of scanning electron microscopy (SEM) microstructures and x-ray patterns of $Cr_{1-x}ZnSb$ revealed that only for $x = 0.14$, a phase-pure compound was observed. For the remaining values of x, impurity phases with different concentrations were obtained. Thus, the following part of the paper focuses on $Cr_{0.86}ZnSb$, and only data and analyses of this sample are presented. A rather spherical single crystal fragment in the range 30–60 μm was isolated from the alloy $Cr_{0.86}ZnSb$, which was additionally heated to 650° C and slowly cooled to 500° C. X-ray intensity data were collected at room temperature on a four-circle APEX II diffractometer [25] equipped with a CCD area detector and an Incoatec Microfocus Source IμS (30 W, multilayer mirror, Mo $K\alpha$; $\lambda = 0.071069$ nm; detector distance of 40 mm; full sphere; $2^\circ < 2\theta < 70^\circ$).

All samples were ground on SiC papers and polished with Al_2O_3 powders (down to 0.3 μm) via standard procedures to be examined by light optical metallography (LOM) and SEM. The microstructure and chemical composition were analyzed by a Jeol JSM-6460 scanning electron microscope equipped with an energy dispersive x-ray (EDX) detector operated at 20 kV and by a Tescan LYRA 3XMH FEG/SEM scanning electron microscope equipped with an X-Max80 Oxford Instruments EDX detector operated at 20 kV. Quantitative evaluation of compositions was performed with the INCA software [26].

A thin lamella (lateral dimensions of about $9 \times 6\,\mu m^2$) was prepared from the polished sample $Cr_{0.85}ZnSb$ using a focused ion beam (FIB) technique in a TESCAN LYRA 3 XMU FEG/SEM × FIB scanning electron microscope. A Thermo Fisher Scientific Thalos F200i transmission electron microscope (TEM) with FEG operated at 200 kV was employed in diffraction mode, to support information about the crystal structure.

The electrical resistivity in the range from 4.2 to 300 K was measured on cuboids ($8 \times 2 \times 1$ mm³) in a conventional ^{4}He cryostat via a four-probe technique, employing an ac Lake Shore Resistance Bridge 370 AC. The Seebeck coefficient at low temperatures was obtained using the seesaw heating method, as described in Ref. [27]. Above room temperature, the electrical resistivity and the Seebeck coefficient were measured simultaneously with a ZEM-3 apparatus (ULVAC-Riko, Japan). The error for both resistivity measurements as well as for the Seebeck coefficient is about 5%. For specific heat measurements, a Quantum Design PPMS was employed for temperatures from 2 to 300 K. Apiezon-N grease served to ensure a good thermal contact between sample and sample platform. Temperature- and field-dependent magnetization data were collected at temperatures ranging from 2 to 350 K using a Quantum Design PPMS with the vibrating sample magnetometer (VSM) option.

Muon spin relaxation (μSR) experiments were performed with the EMU spectrometer at the ISIS neutron and muon spallation source at the Rutherford Appleton Laboratory, United Kingdom [28]. Muons are implanted and thermalized within few picoseconds in the $Cr_{0.86}ZnSb$ sample and a minor fraction in the Ag sample holder and decay with a half-life $\tau_\mu = 2.2\,\mu s$ into positrons. The latter are emitted with an asymmetric probability with respect to the muon spin orientation. The muon spin polarization, thus, corresponds to the measured asymmetry between positron counts in forward and backward detectors (in so-called longitudinal detector geometry). Based on a statistic of typically 2×10^7 muon decays, the asymmetry is determined as a function of time. Zero-field μSR measurements were taken in temperature steps of 10 K ranging from 20 to 240 K and at 300 K. At the latter temperature, additional 20 G transverse field data were collected to calibrate the relative efficiency of the forward and backward detectors. Accordingly, an initial asymmetry of approximately 27% refers to a perfect spin polarization of the implanted muons parallel to the beam forward direction. We used the WIMDA software [29] for analyzing the μSR data.

B. Computational aspects

For the DFT calculations, the Vienna *Ab initio* Simulation Package (VASP) [30,31] with the projector augmented wave

(PAW) potential construction [32,33] was applied. The Zn pseudopotential was constructed by treating the $3d^{10}$ and $4s^2$ states as valence states, whereas for Sb the pseudopotential included the $5s^2$ and $5p^3$ states as valence states. For the Cr pseudopotential construction, the atomic orbital configuration $3s^2\,3p^6\,3d^5\,4s^1$ was used. A plane wave basis cutoff of 600 eV was chosen, ensuring highly converged results with respect to basic functions. Dense k-point grids were constructed by setting the VASP parameter KSPACING = 0.06 in all calculations. For example, for the perfect $P4/nmm$ structure of $Cr_2Zn_2Sb_2$ it resulted in a grid of $25 \times 25 \times 17$ k points. For the derivation of local (or site-projected) properties such as ℓ-projected densities of states, magnetic moments, and atomlike charges in atomic spheres of radii 0.116 nm for Cr, 0.124 nm for Zn, and 0.158 nm for Sb were allocated to each corresponding atomic position. All crystal structure parameters were fully relaxed by minimizing total energies and atomic forces. Numerous DFT spin-polarized calculations were performed for studying structural stabilities and magnetic structures. All DFT results were obtained employing the standard GGA-PBE ansatz [34] for exchange and correlation without any corrections for additional enhanced exchange-correlation interactions such as the DFT+U approach of Dudarev *et al.* [35]. This approach overestimates the equilibrium volumes and consequently leads to less agreeable results (see Sec. III C). Charge transfer, atomic volumes, and atomlike charges were computed by analyzing the charge density in terms of the quantum theory of atoms in molecules according to Bader *et al.* [36–41]. Applying an adapted version of the BOLTZTRAP package [42], thermoelectric properties such as the Seebeck coefficient and electrical resistivity were computed within Boltzmann's transport theory assuming constant relaxation time.

III. SYNTHESIS AND CHARACTERIZATION

A. Structure and structure stability of $Cr_{0.86}ZnSb$

The x-ray intensity patterns of a single-crystal specimen, extracted from the rim of a sample of $Cr_{0.86}ZnSb$, were fully indexed and were unambiguously consistent with the space group $P4/nmm$ (No. 129, origin at center) and lattice parameters $a = 0.41704(1)$ nm and $c = 0.61855(2)$ nm, $c/a = 1.483$. A structure solution by direct methods indicates isotypism with the structure type of MnAlGe (anti-PbFCl type) as defined for MnZnSb (for details see Pearson's Crystal Data compilation [43]). The refinement, however, documents a significant amount of random defects on the Cr site (0.86(1) Cr in 2a (3/4, 1/4, 0)), a rather small, almost insignificant, amount of defects in the Zn site 2c (1/4, 1/4, $z = 0.27985(10)$; occ = 0.98(1)), and full occupancy on the Sb site in 2c (1/4, 1/4, $z = 0.71853(5)$). Final refinements with anisotropic atom displacement parameters (ADPs) converged to $R_F = 0.0124$ with residual electron densities smaller than $\pm 1.37\,e^- \times 10^{-3}$ nm^3. The crystallographic data are summarized in Tables I(a) and I(b), including interatomic distances, which are consistent with the sum of CN12 metal atom radii (CN is the coordination number; $R_{Cr} = 0.1360$ nm, $R_{Zn} = 0.1394$, and $R_{Sb} = 0.1590$ nm [46]). A quantitative Rietveld refinement of the x-ray powder intensities of $Cr_{0.86}ZnSb$ ($R_F = 0.055$; see Fig. 1) clearly confirms the structure as derived from the single-crystal study, as well as the Cr defects. The structure model of $Cr_{0.86}ZnSb$ ($\equiv Cr_{30.1}Zn_{34.5}Sb_{35.2}$ at. %) is satisfactorily refined and in excellent agreement with the composition of $Cr_{30.9}Zn_{33.8}Sb_{35.3}$ at. %, as derived from electron probe microanalysis (EPMA) (see inset in Fig. 1). It should be emphasized that the least-squares structure refinement did not accept extra Sb at either the Cr site or the Zn site.

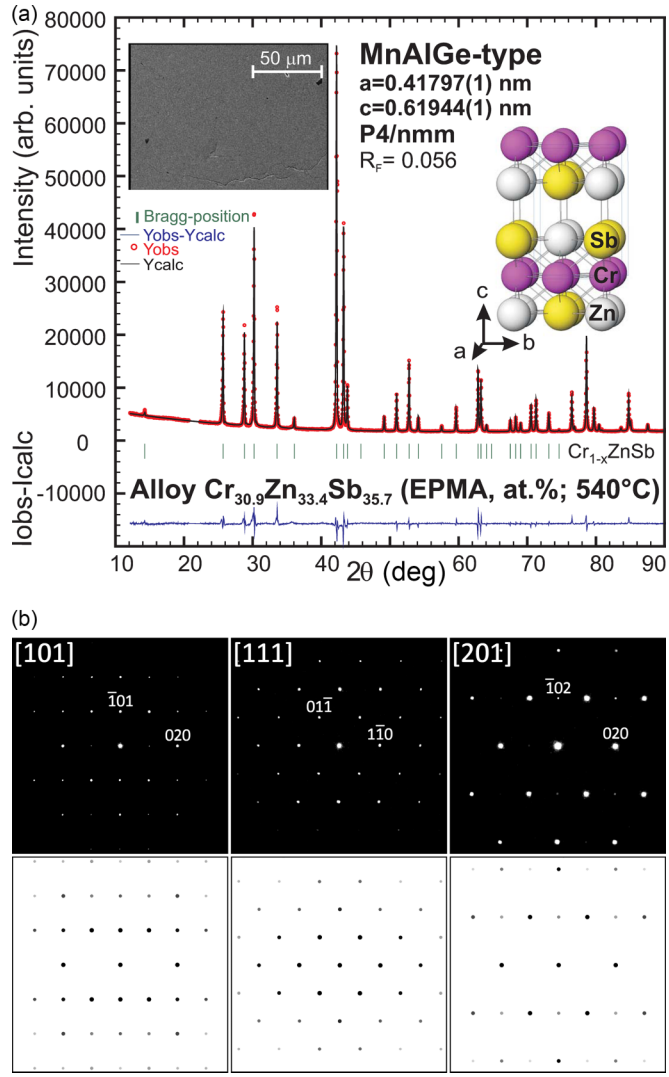

FIG. 1. (a) Rietveld refinement for $Cr_{1-x}ZnSb$; $x = 0.14$ (left inset, EPMA backscatter micrograph; right inset, structure of $Cr_{0.86}ZnSb$ in three-dimensional view: violet, Cr atoms; light grey, Zn atoms; and yellow, Sb atoms). (b) Selected area electron diffraction (SAED) patterns of $Cr_{0.86}ZnSb$ at various sample tilts together with the results of kinematic simulation.

The structure of $Cr_{0.86}ZnSb$, as shown in Fig. 1, can be viewed as a sequence of densely packed but defect Cr layers in the (a, b) plane (with direct Cr-Cr distances $d_{Cr-Cr} = 0.29489$ nm) stacked along the c axis with two Zn/Sb layers in between. While Cr-Zn, Cr-Sb and particularly Zn-Sb distances are consistent with the sum of radii, the structural arrangement also induces a long distance for

TABLE I(a). X-ray single crystal and powder data for $Cr_{0.86}ZnSb$; MnAlGe-type, space group $P4/nmm$, No. 129 (origin at center). The crystal structure was solved with programs SHELXS-97, SHELXL-97-2 within the program OSCAIL [44]. Finally, the crystal structure was standardized with the program Structure Tidy [45]. (b) Interatomic distances (< 0.4 nm) for single-crystal data of $Cr_{0.86}ZnSb$.

Parameter/compound	$Cr_{1-x}ZnSb$ (Rietveld)	$Cr_{1-x}ZnSb$ (single crystal)
Composition from EPMA in at. %	Cr30.9Zn33.8Sb35.3	Cr30.9Zn33.8Sb35.3
Formula from refinement in at. %	Cr30.1Zn34.9Sb35	Cr30.1Zn34.5Sb35.2
Formula from refinement	$Cr_{0.86}ZnSb$	$Cr_{0.86}Zn_{0.98}Sb$
Radiation	Cu $K\alpha_1$ (Guinier)	Mo $K\alpha$ (APEX II)
2θ range (deg)	$18 \leqslant 2\theta \leqslant 100$	$2 \leqslant 2\theta \leqslant 72.7$
Linear absorption coefficient in mm^{-1}		27.16
Density in Mg/m^3	7.34	7.13
$a = b$, c; all in nm	0.41797(1); 0.61944(1)	0.41704(1); 0.61855(2)
Reflections in refinement (total)	51	178 Fo > 4σ (Fo) (5710)
Number of variables	24	12
$R_F = \Sigma\|F_o - F_c\|/\Sigma F_o$	0.0549	210 frames (5 sets)
$R_I = \Sigma\|I_o - I_c\|/\Sigma I_o$	0.0760	Redundancy > 8
$R_{wP} = [\Sigma w_i\|y_{oi} - y_{ci}\|^2/\Sigma w_i\|y_{oi}\|^2]^{1/2}$	0.0412	$R_F^2 = \Sigma\|F_0^2 - F_c^2\|/\Sigma F_0^2 = 0.0124$
$R_P = \Sigma\|y_{oi} - y_{ci}\|/\Sigma\|y_{oi}\|$	0.0618	$wR2 = 0.0288$
$R_e = [(N-P+C)/(\Sigma w_i y^2{}_{oi})]^{1/2}$	0.0182	$R_{int} = 0.026$
$\chi^2 = (R_{wP}/R_e)^2$	11.5	GOF = 1.154
Extinction (Zachariasen)		0.044(2)
Residual density $e^-/nm^3 \times 10^3$; max; min		1.37 (0.065 nm from Zn), −0.93
Atom positions		
Cr: 2a ($\frac{3}{4}$, $\frac{1}{4}$, 0); Occ.	0.86(1) Cr	0.863(4) Cr
$U_{11} = U_{22}$; U_{33}; $U_{23} = U_{13} = U_{12} = 0$	Biso = 0.47	0.0131(3); 0.0067(3)
Zn: 2c ($\frac{1}{4}$, $\frac{1}{4}$, z); Occ.	1.0(-) Zn	0.983(4) Zn
z	0.2814(4)	0.27985(10)
$U_{11} = U_{22}$; U_{33}; $U_{23} = U_{13} = U_{12} = 0$	Biso = 0.59	0.0163(2); 0.0176(3)
Sb: 2c ($\frac{1}{4}$, $\frac{1}{4}$, z); Occ.	1.00(-) Sb	1.00(-) Sb
Z	0.7175(2)	0.71853(5)
$U_{11} = U_{22}$; U_{33}; $U_{23} = U_{13} = U_{12} = 0$	Biso = 0.32	0.0104(1); 0.0101(1)
Cr	−4 Zn	0.27101
	−4 Sb	0.27164
	−4 Cr	0.29489
Zn	−4 Cr	0.27101
	−1 Sb	0.27135
	−4 Sb	0.29489
Sb	−1 Zn	0.27135
	−4 Cr	0.27165
	−4 Zn	0.29489

the Cr-Cr interaction along the c direction (0.61855(2) nm). This geometry may severely affect the magnetic properties (see below). Coordination figures are simple tricapped triangular prisms for Zn and Sb (coordination number CN = 9) and a cuboctahedron for Cr (CN = 12). No homogeneity region in the direction of a full Cr occupancy was detected.

Selected area electron diffraction (SAED) patterns were collected by TEM from thin lamellas of the $Cr_{0.86}ZnSb$ sample (see Fig. 1, lower panel). All diffraction patterns were fully indexed using the parameters of the tetragonal lattice obtained from the single-crystal refinement (Table I(a)). No further superstructure spots were detected; thus no ordering exists among the randomly distributed Cr atoms and vacancies. The lower panel in Fig. 1 shows several examples of low index zone axis diffraction patterns recorded at various sample tilts, together with simulated SAED patterns using the software JEMS [47,48].

B. DFT structures for $Cr_2Zn_2Sb_2$ (C-AF) and $Cr_4Zn_4Sb_4$ (G-AF)

In the following section, two types of DFT-derived antiferromagnetic ground states (C-AF and G-AF) are discussed. Both orderings feature a checkerboard pattern in the ($\vec{a}$, $\vec{b}$) plane, depicted in Fig. 2(c) [11]. The difference between the two structures is the ordering in the $\vec{c}$ direction. For C-AF, the Cr moments are ordered parallel, while for G-AF ordering, an alternating up-down magnetic ordering occurs along $\vec{c}$, doubling the unit cell in the $\vec{c}$ direction [see Figs. 2(a) and 2(b)]. For the C-AF structure of $Cr_2Zn_2Sb_2$, antiferromagnetic ordering occurs in the ($\vec{a}$, $\vec{b}$) plane [Fig. 2(b)].

Table II lists the DFT-derived atomic coordinates of the C-AF structure revealing the peculiar, layered properties of the $P4/nmm$ structure: (a) Cr atoms in the ($\vec{a}$, $\vec{b}$) plane, which are sandwiched between mixed Zn-Sb planes, (b) Cr atoms in chains in the $\vec{c}$ direction alternating with Zn-Sb chains, and

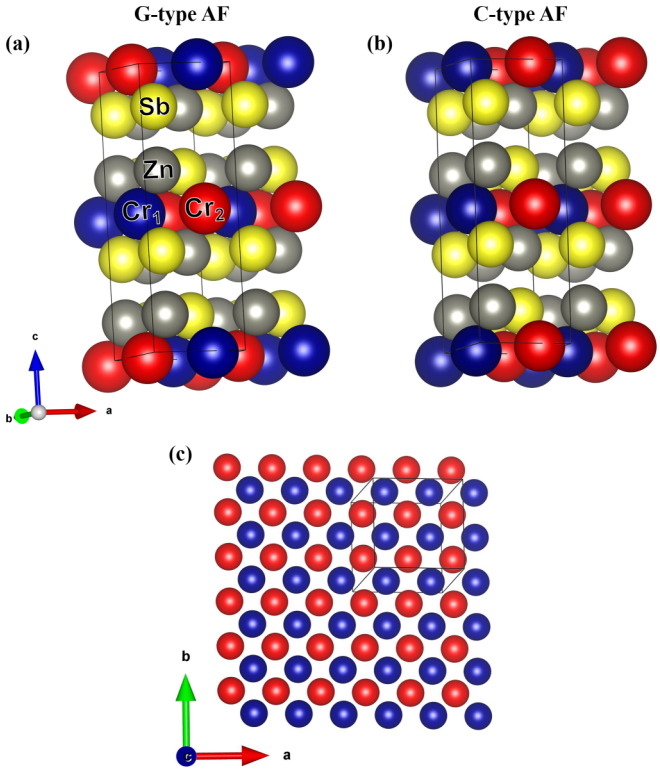

FIG. 2. Sketch of the tetragonal MnAlGe $P4/nmm$ structure of $Cr_2Zn_2Sb_2$ with $c/a = 1.492$ doubled in the c direction (plotted by VESTA [50]) in (a) G-type AFM and (b) C-type AFM magnetic ordering. (c) Cr atoms in the ($\vec{a}$, $\vec{b}$) plane with checkerboard antiferromagnetic ordering [11]. Red and blue spheres refer to spin-up and spin-down Cr magnetic moments, respectively.

(c) empty layers without Cr atoms. The same holds for the G-AF structure, for which there is now antiparallel magnetic moment ordering in the $\vec{c}$ direction.

For the G-AF spin configuration, Fig. 2(a) sketches the unit cell of $Cr_4Zn_4Sb_4$ (C-AF, doubled in the c direction). For

TABLE II. DFT-derived structural data for $Cr_2Zn_2Sb_2$ with $P4/nmm$ structure and C-AF antiferromagnetic ordering. Lattice positions corresponding to the lattice parameters $a = 0.4206$ nm and $c = 0.6277$ nm. For $Cr_4Zn_4Sb_4$ with G-AF ordering the lattice positions are very similar but for comparison the z coordinates have to be divided by 2 because of the doubling of the cell in the c direction. The second $Cr_2Zn_2Sb_2$ unit, which is ordered with antiparallel magnetic moments to the first unit, is constructed by adding (0,0,0.5) to the positions of the first unit. The lattice parameters for G-AF are $a = 0.4253$ nm and $c = 2 \times 0.6175$ nm.

$Cr_2Zn_2Sb_2$ C-AF			
Atom	x	y	z
Cr1	0.75	0.25	0
Cr2	0.25	0.75	0
Zn1	0.25	0.25	0.273
Zn2	0.75	0.75	−0.273
Sb1	0.25	0.25	−0.287
Sb2	0.75	0.25	0.287

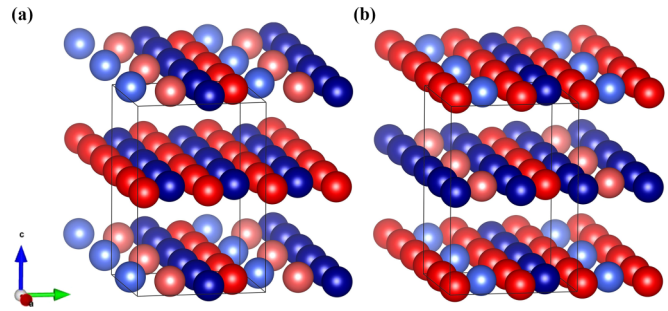

FIG. 3. DFT structures with two Cr vacancies per 46-atom supercell. Only spin-up and spin-down (red and blue) Cr atoms are shown. (a) *vac*1-9 structure with C-AF ordering. (b) *vac*1-2 structure with G-AF ordering. Atoms in vacancy rows appear in lighter colors.

G-AF in the $\vec{c}$ direction the checkerboard layers are repeated with reversed magnetic moments. The energy difference between C-AF and G-AF is rather small, with G-AF being more stable by 0.59 kJ mol^{-1} ($Cr_2Zn_2Sb_2$). Noticeable for the G-AF structure in comparison to C-AF (see caption of Table II) there is a contraction of the lattice parameter c by 1.6% and a stretching of a by about 1.1%.

To obtain a deeper understanding of the chemical bonding, also charge transfer was calculated for stoichiometric $Cr_2Zn_2Sb_2$ and is presented in the Supplemental Material [49].

C. DFT vacancy structures of $Cr_{0.875}ZnSb$

As discussed in Sec III A, the experimentally synthesized compound does not crystallize defect-free; rather the stable stoichiometry was found to be $Cr_{0.86}ZnSb$. Subsequently, structures with a stoichiometry of $Cr_{0.875}ZnSb$ were modeled, constructing supercells with composition $Cr_{14}Zn_{16}Sb_{16}$. The simplest ansatz for a Cr-vacancy structure with a composition close to experiment would be $Cr_7Zn_8Sb_8$, which, however, does not allow for perfect antiferromagnetic ordering, as the supercell contains an odd number of magnetic Cr atoms. To maintain a zero total magnetic moment for the modeled crystal, a $2 \times 2 \times 2$ supercell containing 16 atoms per species was constructed, allowing to remove a suitable pair of antiparallel magnetic Cr atoms, resulting in $Cr_{14}Zn_{16}Sb_{16}$ with a zero total magnetic moment.

In general, the formation of Cr vacancies is supported by our DFT calculations, which result in an energy difference of 2.4 kJ mol^{-1} (CrZnSb), by which G-AF-ordered $Cr_{14}Zn_{16}Sb_{16}$ plus two Cr atoms arranged in a bcc structure is more favorable than vacancy-free $Cr_{16}Zn_{16}Sb_{16}$ with G-AF ordering. For the vacancy supercells, G-AF ordering was found to be more stable than the respective C-AF structures. The differences, however, are rather small—a fraction of 1 kJ mol^{-1} ($Cr_{0.875}ZnSb$). For G-AF ordering, the two most stable atomic arrangements are depicted in Fig. 3. For *vac*1-2 G-AF in Fig. 3(a), one observes rows with vacancies alternating with defect-free rows in the ($\vec{a}$, $\vec{b}$) plane. Along $\vec{c}$, this distribution is repeated but with up-down moments reversed. Figure 3(b) illustrates the *vac*1-9 G-AF structure, with two neighboring defect rows in the ($\vec{a}$, $\vec{b}$) plane. Along $\vec{c}$, an ($\vec{a}$, $\vec{b}$) plane with defect rows alternates with defect-free planes.

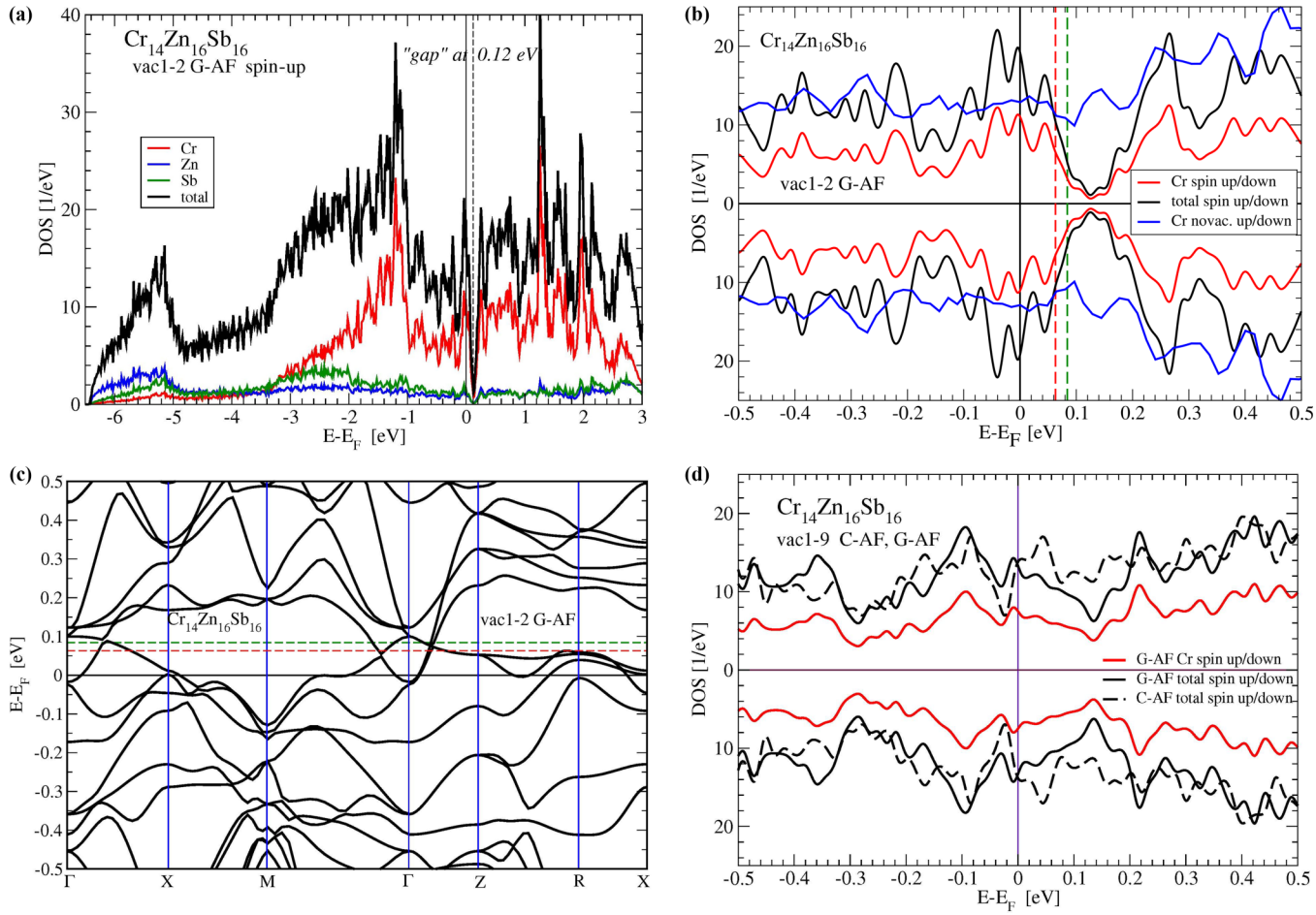

FIG. 4. (a) Spin-up DOS of *vac*1-2 G-AF. The DOS for only one spin direction is shown; because of symmetry the DOS is the same for the second spin direction. Local densities of states summed over all ℓ for Cr (red), Zn (blue), and Sb (green). (b) DOS close to E_F for G-AF ordered *vac*1-2 $Cr_{14}Zn_{16}Sb_{16}$ and stoichiometric CrZnSb. The black, red, and blue lines refer to the total DOS, the local DOS for Cr, and the total DOS for the vacancy-free G-AF structure, respectively. (c) Band structure of *vac*1-2 near the Fermi level. The dashed lines again refer to E_F for the two doping levels. (d) DOS close to E_F for *vac*1-9 for C-AF (dashed line) and G-AF (solid lines) ordering.

As the formation energies are rather similar, a DFT prediction of the most stable structure is not unambiguous. Interestingly, however, the two discussed structures exhibit distinctly different electronic density of states (DOS) features close to Fermi energy, of which only *vac*1-2 G-AF satisfactorily reproduces the measured transport properties (see Sec. V).

For the *vac*1-2 G-AF structure with composition $Cr_{1.75}Zn_2Sb_2$ the DFT equilibrium volume is $0.1096\,nm^3$, which compares favorably with the slightly smaller experimental volume of $0.1082\,nm^3$ for $Cr_{1.72}Zn_2Sb_2$. The DFT lattice parameters of the supercell, $a/2 = 0.4216$ nm and $c/2 = 0.6166$ nm, are in good agreement with the experimental data of $a = 0.418$ nm, $c = 0.619$ nm. The DFT volume for $Cr_2Zn_2Sb_2$ without vacancies of $0.1115\,nm^3$, however, is larger than the vacancy value by about 1.7%. Switching on a DFT+U approach [35] for the Cr d states increases the equilibrium volumes of the *vac*1-2 G-AF structure by 2.4% ($U - J = 1$ eV), 4.9% ($U - J = 2$ eV) and 7.4% ($U - J = 3$ eV). Clearly, such an approach (even for a rather modest value of $U - J = 1$ eV) is not advisable for deriving a correct ground-state volume.

Because the measured samples are synthesized at elevated temperatures, a suitable thermodynamic average of the relaxed supercell structures needs to be considered for a comparison of structural details. It can, however, be safely assumed that the small distortions of lattice coordinates upon vacancy formation—as they appear in the relaxed DFT calculations—average out. On the other hand, the average must ensure in some way the dominance of the pseudogap feature as seen in the DOS of *vac*1-2 G-AF, because of the agreement of measured and calculated electronic transport properties reported in Sec. V.

D. DFT electronic structure of $Cr_{0.875}ZnSb$

All DOS calculations were performed for antiferromagnetic ordering. All the total spin-up and spin-down DOS, summed over all atoms of the Cr, Zn, and Sb sublattices, are the same for both directions. The local atomic DOS contributions are the sum over all the ℓ-projected DOS contributions within a sphere surrounding each species of atom (see Sec. II B). The spin-up DOS for the *vac*1-2 G-AF structure in Fig. 4(a) shows distinct features below −3 eV, where Zn

s-like and Sb *p*-like states dominate. Then, hybridization with Cr states sets in and above −2 eV the DOS is dominated by Cr *d*-like states up to 2 eV.

A striking pseudogaplike minimum forms right above the Fermi level at $E_{gap} = 0.12$ eV. A closer look [see Fig 4(b)] illustrates the rapid fall and rise of the DOS above and below E_{gap}. If E_F is shifted up to E_{gap} then two electrons (one spin-up and one spin-down) need to be doped to the vacancy system. This gaplike feature occurs, even when the structure is not relaxed; therefore, it cannot be explained by structural relaxation as caused by the vacancies. It also exists if perfect antiferromagnetic ordering is destroyed, as revealed by a DFT calculation for a $Cr_7Zn_8Sb_8$ vacancy supercell (see Fig. S1 of theSupplemental Material [49]). For that, the unit cell of perfect $Cr_2Zn_2Sb_2$ was doubled in the $(\vec{a}, \vec{b})$ plane resulting in $Cr_8Zn_8Sb_8$, which, by removing one spin-up Cr atom, ends up in $Cr_7Zn_8Sb_8$. Because of the removed spin-up Cr atom, the total magnetic moment is now $-3.47\,\mu_B$. This vacancy structure is energetically less stable by only 0.61 kJ mol^{-1} ($Cr_{0.875}ZnSb$) than the perfect antiferromagnetic *vac*1-2 AFB structure. Inspecting the DOS, one detects again a similar deep gaplike feature at −62 meV now below E_F (see Fig. S1 of the Supplemental Material [49]).

In Fig. 4(b), by comparing the DOS of the vacancy-free $Cr_{16}Zn_{16}Sb_{16}$ structure with the pseudogap case, the effect of the vacancies is strikingly illustrated: at the energy of the pseudogap, a peak of the DOS of the vacancy-free case arises. Figure 4(c) depicts the band structure of *vac*1-2 G-AF. The red and green dashed lines mark the positions of the two doping energies as discussed in Sec. V. Noticeably, at E_F up to 0.15 eV the number of bands along Γ-X-M-Γ is strikingly reduced compared to energies below.

Figure 4(d) depicts the densities of states of a different vacancy structure *vac*1-9 for G-AF and C-AF, respectively. For this structure, no pseudogap is discernible, as the calculations reveal a metallic density of states close to E_F. Notably, this disagrees with the experimental results displayed in the subsequent sections.

Analyzing the bonding of the states around E_F for the perfect structure $Cr_{16}Zn_{16}Sb_{16}$, one finds Cr *d* states with predominantly d_{xz} and d_{yz} character which interact with Sb *p* states of p_z character. The Cr-Zn and Cr-Sb bond lengths of 0.271 nm [Table I(b)] are the shortest of the compound. Part of these $p-d$ bonds are broken, when Cr vacancies are introduced. This bond breaking also happens for all the Cr-vacancy structures, but an expressed gaplike feature in the DOS appears only for the *vac*1-2 G-AF structure. There, chains of Cr vacancies in the $\vec{c}$ direction are formed. Further analysis shows also *s*-like and smaller *p*-like DOS features for Zn.

As elaborated in Sec. V, a distinct feature of the measurement data is the temperature-dependent Seebeck coefficient, with a maximum of 64 μV K^{-1} at around 178 K. The electronic structure and DOS at E_F cannot explain such a high Seebeck coefficient. Rather, the Fermi energy needs to be shifted closer to the gaplike feature by an electron doping of $1.46\,e^-$ for a composition of $Cr_{14}Zn_{16}Sb_{16}$, yielding reasonable agreement with our measurements (see Sec. V B). Then, E_F lies 62 meV above the undoped case.

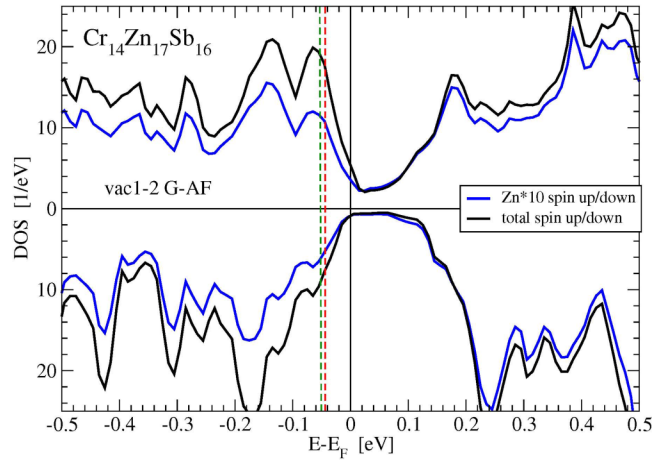

FIG. 5. Electronic DOS close to E_F of $Cr_{14}Zn_{17}Sb_{16}$. One Zn atom is placed at a spin-up Cr-vacancy site of the *vac*1-2 G-AF structure. Red and green dashed vertical lines indicate the respective Fermi energies of positive doping by removing 0.6 and 0.76 electrons. The total spin-polarized DOS (black line) and the corresponding local Zn DOS (blue line, summed over all Zn atoms), enlarged by a factor of 10, are shown.

E. Consideration of different defects

Inspecting the DOS of Fig. 4(b) of the vac1-2 G-AF structure, one finds the discussed minimum at exactly two electrons above the Fermi energy. An additional Zn atom with two valence electrons would place E_F in the pseudogap, which is confirmed by the self-consistent calculation for one Zn atom placed at a Cr-vacancy site, yielding a stoichiometry of $Cr_{14}Zn_{17}Sb_{16}$. Figure 5 shows the DOS of the fully relaxed structure. Evidently, E_F is located right below the pseudogap regarding the spin-up and spin-down DOS, which are different, because the corresponding symmetry, i.e., perfect antiferromagnetism, is destroyed. A small total magnetic moment of about $0.01\,\mu_B$ results. Placing the Zn atom at the second Cr-vacancy site instead, the spin-dependent DOS are reversed. Another effect of the shift of E_F into the pseudogap is the stabilization of the *vac*1-2 G-AF structure, which becomes more stable than the competing *vac*1-9 G-AF structure by 0.54 kJ mol^{-1} ($Cr_{0.875}Zn_{1.0625}Sb$). The magnitude and distribution of the site-projected local moments of Cr are similar to the results for $Cr_{14}Zn_{16}Sb_{16}$.

Figure 5 also shows two more Fermi energies determined by positive doping (less electrons) of 0.6 and 0.76 electrons, cutting through the steep descending slope of the DOS next to the pseudogap. An adjustment of the Fermi energy is necessary to align the transport properties with experiments (see Sec. V). The figure also highlights that the features of the local DOS of Zn near E_F closely follow the total DOS, indicating hybridization of the states close to the pseudogap.

Another defect structure was studied for $Cr_{14}Zn_{15}Sb_{17}$ by substituting a Zn atom with Sb next to a Cr vacancy. The analysis of the DOS again displays the hallmark of the pseudogap which appears about one electron above E_F. For a doping of 0.5 electron, the temperature-dependent Seebeck coefficient and resistivity were calculated and reveal similar behavior to the experimental results. Because the DOS minimum is less

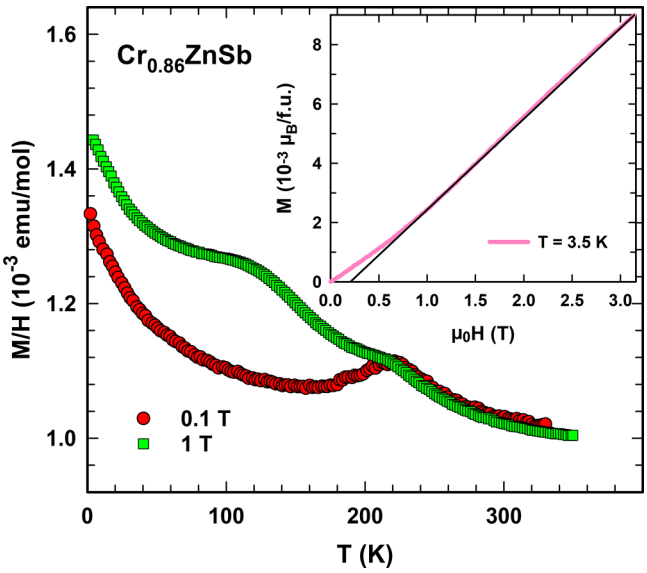

FIG. 6. Temperature-dependent magnetic susceptibility, $M/H(T)$, of $Cr_{0.86}ZnSb$ measured at applied fields as labeled. The inset shows isothermal magnetization data, $M(H)$, measured at 3.5 K. The straight black solid line is a linear fit to M ($H > 1$ T) intended to uncover the nonlinear field dependence of the isothermal magnetization at fields below 1 T.

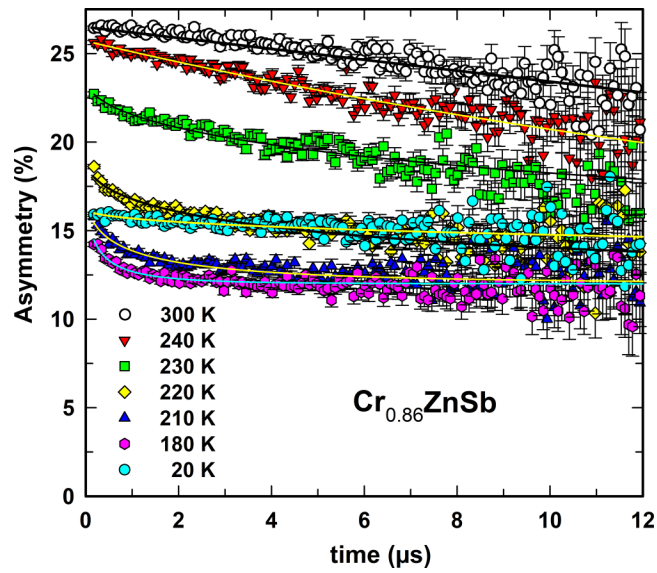

FIG. 7. The time-dependent zero-field μSR asymmetry data of $Cr_{0.86}ZnSb$ at selected temperatures as labeled, with fits shown as solid lines (see text).

steep in comparison with the previously discussed cases, the maximum of the positive Seebeck peak is significantly lower. Similar to $Cr_{14}Zn_{17}Sb_{16}$, the antiferromagnetism is not perfect anymore because of the symmetry reduction, and therefore a small total moment of $-0.03\,\mu_B$ arises.

Based on the defect investigations, it is conceivable that the real system includes a mixture of defect structures. For example, a mixture of $(1-x)(Cr_{14}Zn_{15}Sb_{17}) + x(Cr_{14}Zn_{17}Sb_{16})$ would result in $Cr_{0.857}ZnSb$ for $x = 2/3$, which is very close to the experimental data.

IV. MAGNETIC PROPERTIES

Magnetic susceptibility and specific heat measurements of a nominally stoichiometric CrZnSb sample were reported by Ciesielski *et al.* [11]. Their magnetic susceptibility data revealed a distinct anomaly near 230 K, which, however, was attributed to antiferromagnetic ordering of an unspecified impurity phase, and the intrinsic magnetic behavior of CrZnSb was concluded to be paramagnetic.

A. Magnetic susceptibility and magnetization studies

The temperature-dependent dc magnetic susceptibility of $Cr_{0.86}ZnSb$, $\chi(T) \equiv M/H(T)$, measured at an applied field $\mu_0 H = 0.1$ T (Fig. 6), reveals an antiferromagnetic-like cusp at $T_N \sim 220$ K, which is superimposed to a rather large, weakly temperature-dependent Pauli-like susceptibility, $\chi_0 \sim 10^{-3}$ emu/mol. Despite slightly different nominal stoichiometries of the present $Cr_{0.86}ZnSb$ sample as compared to earlier reported CrZnSb, we observe a very close match of the 0.1 T susceptibility data with those shown in Ref. [11] and we, thus, assign the revealed features of the magnetic susceptibility to an intrinsic behavior of the $Cr_{0.86}ZnSb$ matrix phase. An itinerant, weak-antiferromagnetic nature of the magnetic state of $Cr_{0.86}ZnSb$ is indicated by the large T-independent contribution χ_0 and by a superlinear field dependence of the isothermal magnetization M(H), measured at low temperature ($T = 3.5$ K) and displayed as an inset of Fig. 6. The latter is indicative of a broadened metamagnetic transition, occurring at fields up to 1 T. As revealed in Fig. 6 by a distinct difference between M(T)/H curves measured at 0.1 and 1 T, an initially nonlinear field dependence of the magnetization persists for temperatures up to $T_N \sim 220$ K.

The temperature-dependent heat capacity $C_p(T)$ of $Cr_{0.86}ZnSb$, as depicted in Fig. S3 of the Supplemental Material [49], reveals a small anomaly around 220 K, which is in good agreement with an itinerant antiferromagnetic phase transition, aligning with the magnetic susceptibility data. From the low-temperature data of $C_p(T)$, we further determined a Sommerfeld coefficient of $\gamma = 10.7(5)$ mJ mol^{-1} K^{-2}. DFT-derived values of γ are notably lower, indicating an effective mass enhancement due to spin fluctuations as detailed in the Supplemental Material [49].

B. Muon spin relaxation study of the magnetism in $Cr_{0.86}ZnSb$

The rather weak features of antiferromagnetic order revealed by the above magnetic susceptibility and heat capacity results may not be sufficiently conclusive with respect to an intrinsic bulk or extrinsic impurity origin. We, thus, complemented the macroscopic bulk measurements with microscopic local probe μSR studies. The latter were executed at 24 temperature steps in zero external magnetic field, of which seven selected relaxation data are displayed in Fig. 7. μSR data taken in the paramagnetic state of $Cr_{0.86}ZnSb$, i.e., at 300 K, refer to an initial $t = 0$ asymmetry ($A_{initial}$) near 27%, which corresponds to the initially fully spin polarized state of the implanted muons. The dynamic relaxation due to paramagnetic fluctuations of the local magnetic fields at

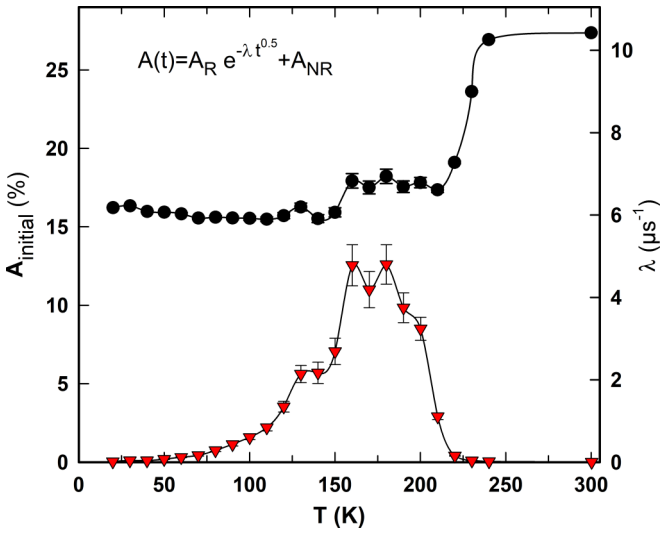

FIG. 8. The temperature-dependent extrapolated initial asymmetry $A_{\text{initial}} = A_{\text{R}} + A_{\text{NR}}$ and muon spin depolarization rate λ of $Cr_{0.86}ZnSb$ resulting from fits with a stretched exponential function with $A_{\text{NR}} = 12\%$ and stretching exponent $\beta = 0.5$ being fixed in a batch fit.

the muon stopping sites in $Cr_{0.86}ZnSb$ are reasonably well accounted for by a simple Lorentzian-type exponential relaxation function. However, at temperatures below 240 K and in particular in the temperature interval 230 to 210 K, dynamic relaxation transforms from a simple exponential to a stretched exponential behavior, $A(t) = A_{\text{R}} \exp(-\lambda t^{\beta})$, on top of a nonrelaxing component, $A_{\text{NR}} \sim 12\%$. The magnitude of the latter component is in realistic correspondence to the spot size of the muon beam and the density of the measured sample for being attributed to the fraction of muons stopping in the sample holder made from Ag metal which displays a negligible zero-field muon spin depolarization. In order to allow us to parametrize the data set over the temperature range 20–300 K, and to avoid correlations between parameters, the function $A(t) = A_{\text{R}} \exp(-\lambda t^{\beta}) + A_{\text{NR}}$ was fitted with A_{NR} fixed at 12% and with the stretching exponent fixed to a constant value $\beta = 0.5$. We note that adjusting these parameters does not affect the essential conclusions discussed below. Obtained fits are shown as solid lines on top of the measured data in Fig. 8. The key feature revealed in Fig. 9 is a steplike temperature-dependent evolution of the extrapolated initial asymmetry, $A_{\text{initial}}(T) = A_{\text{R}}(T) + A_{\text{NR}}$, at around $T_{\text{N}} \sim 220$ K with a truly significant reduction of the extrapolated initial asymmetry A_{initial} from about 27% towards 16%. This corresponds to a loss of roughly two-thirds of the initial signal originating from the sample. Such a steplike evolution of $A_0(T)$ is typical for a state of long-range magnetic order which causes large enough quasistatic magnetic fields at the muon stopping sites to depolarize muons within the initial detector dead time of 0.15 μs following muon implantation at the EMU instrument [28]. The observed dynamic relaxation at $t > 0.15$ μs is attributed to those muon stopping sites where the incoming muon spins are oriented parallel to the local magnetic field and thus remain unaffected by the local magnetic field unless that local field displays transverse magnetic fluctuations. The latter is obviously strongest right below the Néel temperature and slows down at temperatures well below T_{N} (compare the temperature-dependent evolution of relaxation rate $\lambda(T)$ as depicted in Fig. 8). Accordingly, dynamic relaxation effects become almost invisible at 20 K, where $A(t) \sim 16\%$ appears nearly time independent. The strong short-time depolarization effect, which becomes a truly substantial bulk effect at around the Néel temperature $T_{\text{N}} \sim 220$ K, provides clear evidence for the occurrence of intrinsic antiferromagnetic order in $Cr_{0.86}ZnSb$.

C. DFT-derived magnetic properties

The DFT calculation for the non-spin-polarized compound $Cr_2Zn_2Sb_2$ with relaxed $P4/nmm$ structure results in a large value of the DOS at E_{F} as also shown in Ref. [11]. For that,

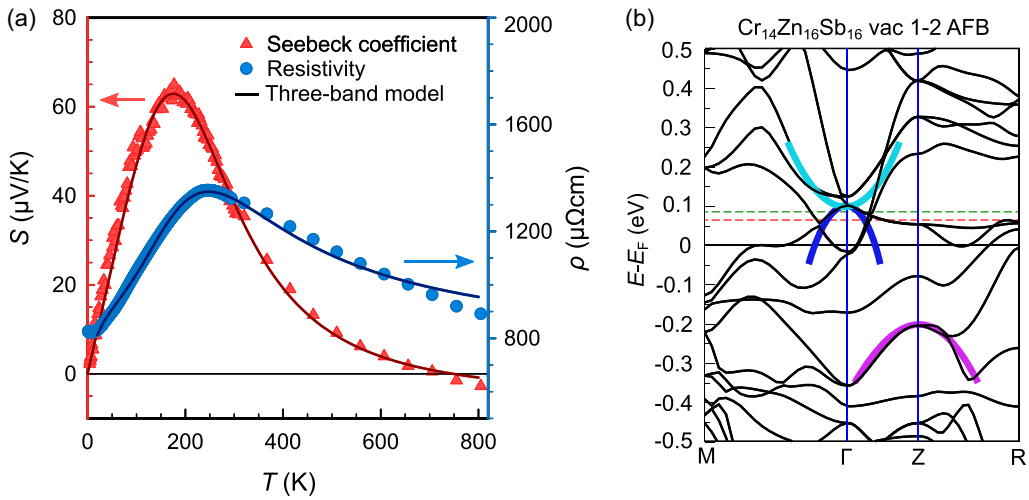

FIG. 9. (a) Temperature-dependent Seebeck coefficient and electrical resistivity of $Cr_{0.86}ZnSb$. Solid lines are least-squares fits employing a parabolic three-band model. (b) DFT-derived band structure of $Cr_{14}Zn_{16}Sb_{16}$, together with a sketch of the band structure (solid, colored lines), obtained from modeling the temperature-dependent Seebeck coefficient of $Cr_{0.86}ZnSb$, employing the three parabolic band model. The red and green dashed lines mark E_{F} for the two doping levels of 1.46 e^- and 1.75 e^-.

Cr d-like states are mainly responsible as reflected by the local DOS of Cr at E_F, N(Cr) $\sim 2\,\mathrm{eV}^{-1}$. On the basis of Stoner's instability criterion for spontaneous ferromagnetic spin polarization, $IN_{Cr}(E_F) > 1$ with an assumed exchange energy for Cr of $I \sim 0.8\,\mathrm{eV}$, it is obvious that the electronic structure of the non-spin-polarized compound $Cr_2Zn_2Sb_2$ is unstable against ferromagnetic spin polarization. The DFT ground-state density is spin polarized and, based on the site-projected spin densities, local magnetic moments are defined at the respective atomic sites. Therefore, comparison with experiment is only meaningful when results of spin-polarized DFT calculations are considered.

Although a ferromagnetic (FM) ground state of $Cr_2Zn_2Sb_2$ is found, which is more stable by $33\,\mathrm{kJ\,mol}^{-1}$ (CrZnSb) than the nonpolarized result, antiferromagnetic (AFM) magnetic orderings need to be studied because of the presence of Cr. Investigating bcc Cr at the calculated equilibrium volume, small magnetic moments with antiferromagnetic ordering in a simple cubic lattice are established, in agreement with the results of Ref. [51]. There, it is mentioned that the energetic proximity of FM and AFM ordering may indicate the formation of a spin-density wave (SDW). According to the present DFT calculations, the energy difference between $Cr_2Zn_2Sb_2$ C-AF and the corresponding FM phase is $\approx 4.8\,\mathrm{kJ\,mol}^{-1}$ (CrZnSb). Formation of SDWs cannot be excluded *a priori*. It is well known that many Cr alloys and compounds reveal SDWs [52]. Also, simple cubic Cr_2 is prone to formation of SDWs below 110 K, which is due to Fermi surface nesting features [51,53]. Nevertheless, the magnetic experimental results of the present work do not indicate any formation of SDWs.

The AFM backbone of Cr_xZnSb is the planar checkerboard arrangement as illustrated in Fig. 2(b). For the DFT-derived planar lattice parameter of $a = 0.4206$ nm for $Cr_2Zn_2Sb_2$ C-AF the four nearest-neighbor distances are stretched by a factor of 1.2 in comparison to the eight nearest-neighbor distances of the simple cubic AFM ground-state structure. Performing a DFT calculation for the stretched simple cubic structure results in large spin-up and spin-down local moments of $\pm 3.1\,\mu_B$ with a very small DOS at E_F. Doing the same for FM ordering with starting local moments of $2\,\mu_B$ leads to zero magnetic moments after self-consistency has been achieved, and the spin polarization breaks down. It should be noted that the sizes and up-down orientations of the self-consistent moments are independent of the starting guess. Consequently, the total energy difference between FM and nonpolarized AFM is therefore very large, being greater than $90\,\mathrm{kJ\,mol}^{-1}$ (Cr). Returning to the AFM checkerboard structure, for the layer of pure Cr the DFT calculation predicts a semiconducting antiferromagnetic insulator with a gap of $\sim$0.1 eV and large local spin-up and spin-down moments of $\sim 3.6\,\mu_B$ as well as total spin-up and spin-down moments of $\pm 6\,\mu_B$, the total magnetic moment being zero (see Figs. S2(a) and S2(b) of the Supplemental Material [49]). A corresponding calculation for the FM case results in local magnetic moments of $3.8\,\mu_B$, very similar to the AFM result, and a total magnetic moment of $5\,\mu_B$. The AFM ordering is now more stable than FM by $32\,\mathrm{kJ\,mol}^{-1}$ (Cr). A very similar energy difference is derived for Cr_{14}, with the *vac*1-2 G-AF structure, when all Zn and Sb atoms are removed. Now for the complete $Cr_{14}Zn_{16}Sb_{16}$ vacancy structure *vac*1-2 G-AF, the AFM-FM total energy difference is strongly reduced to $8.3\,\mathrm{kJ\,mol}^{-1}$ ($Cr_{0.875}ZnSb$). For AFM ordering, site-projected local magnetic moments of Cr are in the range of $2.0\,\mu_B$ to $2.6\,\mu_B$, and for FM in the range of $2.0\,\mu_B$ to $2.2\,\mu_B$. Now, the interactions of Cr $3d$ states with the delocalized Sb $5p$ states have a significant impact. As listed in Table I for the $P4/nmm$ structure, Sb—as well as Zn—has four nearest-neighbor Cr atoms. Ideally, Sb is positioned above the center of a square formed by the four Cr atoms (if the Cr site is not vacant). They are ordered in two pairs of antiferromagnetically arranged Cr atoms. As a consequence, the induced site-projected local magnetic moments in the Sb atomic sphere are zero. This is different for the FM case, for which Sb magnetic moments of $0.08\,\mu_B$ are formed, all of them antiparallel to the parallel moments of the ferromagnetic Cr moments. They are of purely p-orbital-like character. For the delocalized Sb $5p$ states, the field of Cr magnetic moments induces the formation of very weak magnetic moments of opposite orientation. Their delocalized character is also emphasized by the very small local DOS of the Sb $5p$ states. Furthermore, according to the charge transfer analysis of Sec. III C, Sb gains electronic charge, and consequently, in a simple model its atomic potentials get less attractive and the atomic states are more delocalized.

For $Cr_{14}Zn_{16}Sb_{16}$ one might distinguish three different magnetic features. The delocalized Sb $5p$ states form some kind of polarizable electronic cloud between the Cr atoms screening the Cr moments. They seem to respond in a paramagnetic manner to a magnetic field as discussed. Furthermore, a weak antiferromagnetic coupling in the $\vec{c}$ direction (G-AF ordering) of about $0.3\,\mathrm{kJ\,mol}^{-1}$ (CrZnSb) is predicted between the antiferromagnetic Cr layers. Finally, the site-projected local magnetic moments of Cr atoms are large, in the range of $2\,\mu_B$ to $2.6\,\mu_B$ in the chosen atomic sphere of Cr, and they couple antiferromagnetically in the $(\vec{a}, \vec{b})$ plane. These features seem to be reflected by susceptibility measurements (Fig. 6; see also Fig. S11a of Ref. [22]).

The peaks in the susceptibility for $T > 200$ K are attributed to the magnetic order-disorder transition of the AFM-ordered screened magnetic moments of Cr in the $(\vec{a}, \vec{b})$ plane. The predicted very weak interaction in the $\vec{c}$ direction according to G-AF ordering is indicated by a feature in the susceptibility at $T \sim 10$ K (as a peak in Ref. [22] and as a flattening in Fig. 6, red curve).

V. TRANSPORT PROPERTIES

A. Measurements and modeling

Transport properties are important to assess the potential of materials for thermoelectric applications and, furthermore, can give valuable insights into the electronic structure around the Fermi energy. To this aim, the temperature-dependent Seebeck coefficient and electrical resistivity of $Cr_{0.86}ZnSb$ was studied in a broad temperature range (4–800 K), as shown in Fig. 9. The Seebeck coefficient, plotted as red triangles, exhibits a distinct maximum around $T = 180$ K, with values up to $S = 65\,\mu\mathrm{V/K}$. The positive sign of $S(T)$ indicates holes as dominant charge carriers up to high temperatures.

The existence of a distinct maximum, moreover, points towards a second band contributing to transport above this

temperature. The sign change of $S(T)$ at around 700 K marks the temperature where this conduction band outweighs the valence-band contribution to the Seebeck coefficient. The resistivity, plotted as blue circles, shows typical features of a heavily doped semiconductor or semimetal. At very low temperatures $\rho(T)$ saturates to a constant value and rises with rising temperature. At around 250 K a maximum evolves, with negative $d\rho/dT$ for elevated temperatures above, presumably due to an increase of the charge carrier concentration n with temperature. To deepen the understanding of the transport behavior of $Cr_{0.86}ZnSb$, the temperature-dependent Seebeck coefficient and electrical resistivity was calculated within the framework of Boltzmann's transport theory, using a three-parabolic-band model. The model was fitted to the experimental data using a least-squares fit method in a two-step procedure [54]. The fitting results are depicted as solid lines in Fig. 9(a). Since the Seebeck coefficient provides a more direct measure of the electronic structure near the Fermi energy (energy-independent terms cancel in the denominator and numerator of the Boltzmann expression), we begin our analysis with *S(T)*. Assuming acoustic-phonon scattering as the dominant scattering mechanism, the parabolic band model yields for the Seebeck coefficient of a single band [55]

$$S(T) = \frac{k_B}{e}\left[\frac{2F_1(\eta, T)}{F_0(\eta, T)} - \eta\right], \tag{1}$$

where F_i are the Fermi integrals of ith order and $\eta = \mu/k_BT$ is the reduced chemical potential. The electron relaxation time and its energy dependence can be approximated by a power-law relation $\tau \propto N^{-1}(E) = \tau_0 E^{-1/2}$ for acoustic-phonon scattering; here, $N(E)$ is the DOS, which follows $\sim E^{1/2}$ for parabolic bands and τ_0 is an energy-independent prefactor. To obtain the total Seebeck coefficient for multiple bands [Eq. (2)], the single contributions must be weighted with the electrical conductivities of the respective bands, neglecting interband scattering:

$$S_{\text{tot}} = \frac{\sum_{i=1}^{N} S_i\sigma_i}{\sum_{i=1}^{N} \sigma_i}. \tag{2}$$

As demonstrated successfully in studies on different materials, such as Fe_2VAl–based Heusler compounds [56–58] and skutterudites [59], band-specific parameters, such as the size of the band gap or overlap, relative band masses, or the position of the Fermi energy can be extracted by modeling $S(T)$ (see Fig. 9). To validate our model results, we additionally fitted the experimental resistivity data in a broad temperature range, using the model parameters obtained from the Seebeck coefficient fit. In this step, only a single free parameter (constant prefactor) must be included, if the dominant scattering process is set *a priori*. At low temperatures, scattering from (ionized) impurities often dominates $\rho(T)$, while phonon scattering becomes more important at higher temperatures due to the strong temperature dependence of the scattering rate, $\sim T^{3/2}$. Therefore, we accounted for two different scattering processes via Mathiessen's rule (ionized impurities plus phonons), which yields remarkable agreement with experimental resistivity data, when the same band parameters from modeling the Seebeck coefficient are used. The fit results yield a semimetallic band configuration, which best describes the measured transport properties. Here the Fermi level is doped significantly into the first valence band by about 48 meV, while the conduction band overlaps with that band, yielding a tiny pseudogap of around −2 meV. The observable negative curvature of the measurement data at elevated temperatures ($T > 300$ K) is modeled by a second valence band, situated further from the Fermi level at −326 meV. For comparison, the effective electronic structure obtained from our fit is illustrated together with the electronic band structure from DFT in Fig. 9(b). It is important to note that only relative band masses are obtained from the fit; therefore, only the relative curvature of the fitted bands is significant. Good agreement with DFT results for $Cr_{0.875}ZnSb$ is found, when directly comparing the band structure with the assessed bands from the fit. The position of the Fermi level agrees very well with the shifted Fermi level obtained from the DFT calculations. Moreover, the position of the two valence bands aligns very well with theoretical bands. The fitted band overlap at E_F is somewhat smaller than the overlap indicated by DFT, which is understandable considering the multiple conduction bands near the Fermi level. In our model, which includes only three bands, the two conduction bands at the Γ point are represented by a single band located at their combined center of mass. Naturally, the DFT result comprises a large number of bands, not all of which can be considered, when fitting the effective band structure from transport properties.

In summary, our analysis of transport properties strongly suggests the presence of a pseudogap in the electronic structure, corroborating the findings from DFT calculations [see Figs. 4(c) and 4(d)]. Good agreement is found when directly comparing the fitted bands with the DFT calculation close to the Fermi level, corroborating the emergence of a pseudogap in off-stoichiometric $Cr_{0.86}ZnSb$. It is remarkable that the Cr vacancies lead to such a drastic change in the electronic density of states.

To further validate the findings, resistivity and the Hall effect of the annealed sample were measured as a function of the magnetic field from 0 to 9 T in the temperature range from 4 to 300 K. As observable in Fig. 10(a), the Hall resistivity ρ_{yx} is linearly proportional to the applied field and decreases with increasing temperature. In the single-band model, the carrier concentration n is proportional to $1/eR_H$, where R_H is the Hall coefficient derived from the slope of the Hall resistivity. In Fig. 10(b), this value is plotted as a function of temperature. A significant rise of the carrier concentration occurs above 150 K, indicating the contribution of a second band around this temperature. This coincides with the maximum of the Seebeck coefficient, S_{max}, shown in Fig. 9(a) and marked here with a dashed green line at around $T = 180$ K. Clearly, this strong increase of the carrier concentration aligning with S_{max} further confirms of the existence of a pseudogap in this system. The Hall mobility, μ_H [Fig. 10(b), left axis] decreases in an almost linear manner from 4 to 300 K. Notably, the sample exhibits negligible magnetoresistance (MR < 1%) over the whole temperature range, which is plotted in Fig. S4 of the Supplemental Material [49].

B. DFT electronic transport

Electronic transport calculations from DFT require the Kohn-Sham eigenvalues $E(\vec{k})$ on a sufficiently dense grid of $\vec{k}$

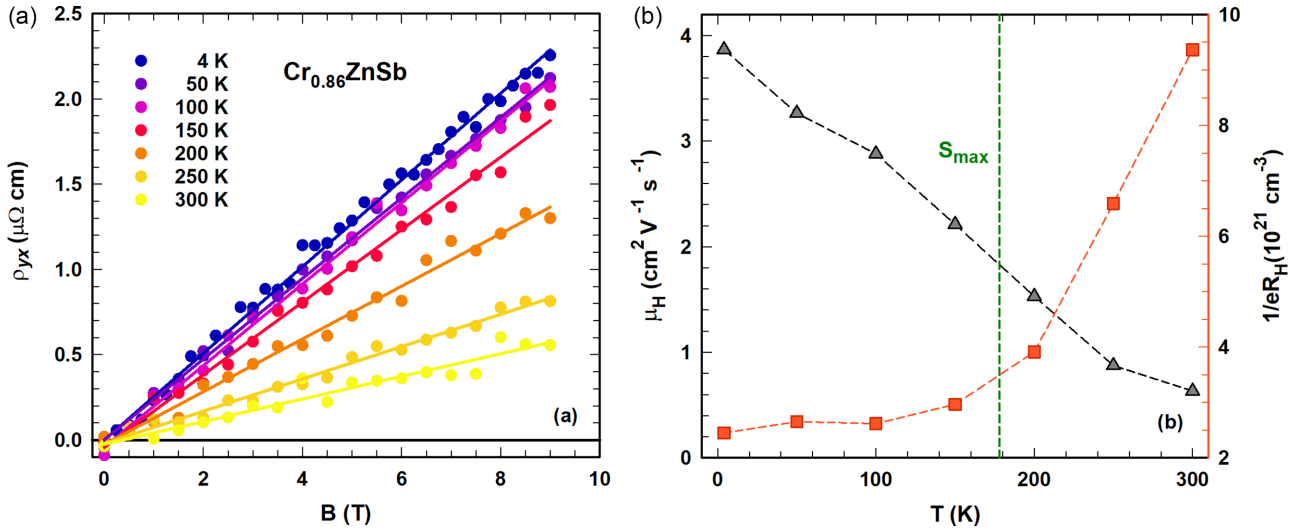

FIG. 10. (a) Field-dependent Hall resistivity of $Cr_{0.86}ZnSb$ for various temperatures. (b) Hall mobility μ_H and $1/eR_H \propto n$ of $Cr_{0.86}ZnSb$. A clear rise of the inverse Hall resistance is found around the Seebeck maximum temperature S_{max} indicating the contribution of a second band to electronic transport around this temperature, consistent with measurements of $S(T)$.

points in the Brillouin zone. Band velocities $\vec{v}(\vec{k}) = \frac{\partial E(k)}{\partial \vec{k}}$, are derived, which appear in integrals over the Brillouin zone including the energy derivative of the Fermi-Dirac distribution:

$$f^{\mathrm{FD}}(E(\vec{k}),\ T,\ \mu) = \left((\exp)\frac{(E(\vec{k}) - \mu)}{k_B T} + 1\right)^{-1}. \quad (3)$$

The Fermi energy E_F at elevated temperatures is the chemical potential μ(T) for the given number of valence electrons. Boltzmann's transport theory requires the integrals $K_{n,ij}$, $i, j = 1, 2, 3$ over the Brillouin zone of the tensor product of band velocities,

$$K_{n,ij} = \frac{1}{4\pi^3\hbar}\int \tau(E(\vec{k}))v_i(\vec{k}) \times v_j\vec{k}(E(\vec{k}) - \mu) \times \left(-\frac{\partial f^{\mathrm{FD}}}{\partial E(\vec{k})}\right)d\vec{k}, \quad (4)$$

involving the relaxation time τ $(E(\vec{k}))$.

Then the components of the electronic conductivity tensor are

$$\sigma_{ij} = e^2 K_{0,ij}. \quad (5)$$

The resistivity tensor $\rho_{ij} = \sigma_{ij}^{-1}$ is the inverse of the conductivity tensor. The relaxation time τ [31] is determined by adjusting the isotropic DFT value to the measured isotropic resistivity at a chosen temperature.

Within the Boltzmann approach, the Seebeck tensor is defined by

$$S_{ij} = \frac{K_{1,\,ij}}{eTK_{0,ij}}, \quad (6)$$

where e is the charge of an electron. In this expression, the constant relaxation time τ cancels out.

Considering a tetragonal crystal symmetry—as is the case in the present study—the resistivity tensor and Seebeck tensors are diagonal and have three nonzero diagonal components $\rho_{ij} = \rho_{22}, \rho_{33}$ and $S_{11} = S_{22}, S_{33}$. The isotropic quantities ρ, S are the averages of the three diagonal elements.

As shown in Fig. 11(a), the measured Seebeck coefficient S_{expt} is positive up to temperatures of 700 K with a pronounced maximum of S_{expt} (178 K) = 64 μV/K. In comparison, the DFT result S_{DFT} for the undoped case shows a broad positive peak with a maximum of ∼ 40 μV/K at ∼ 400 K. It always remains positive even at high temperatures. Clearly, the agreement with S_{expt} is very poor; only the positive signs agree. According to Eqs. (1) and (2), S is positive when states with energies $E(\vec{k})$ lower than μ dominate. Figure 11(b) shows that for the undoped case E_F lies in an energy region where the DOS $N(E_F)$ has a weak negative slope $N'(E_F)$. According to the low-temperature approximation $S \propto -\frac{N'(E_F)}{N(E_F)}$, the sign of S is then positive, which agrees with measurement; however, S is too small, because the ratio is too small. The situation changes when 1.46 electrons are doped to the system. This value was chosen for achieving good agreement with experiment. Then, at the corresponding Fermi energy [red dashed line, Fig. 4(b)], the slope gets more negative, whereas the DOS decreases. Accordingly, S should be larger than for the undoped case. The result of the full DFT calculation [red line in Fig. 11(a)] corroborates this argument: S_{DFT} shows now a large peak of S (234 K) = 78 μV/K. Overall, the DFT result for this doping agrees reasonably well with S_{expt}, even more so when the zero-line crossings at the same temperature, T = 704 K, are taken into account. The tetragonal splitting of the Seebeck tensor components can be quite substantial. For example, for the maximum at T = 234 K it is $S_{11} = S_{22}$ = 95 μV/K and S_{33} = 42 μV/K.

Increasing the electron doping to 1.75 electrons per supercell, the Fermi energy is further increased [green dashed line, Fig. 4(b)] cutting the steep DOS at a reduced value $N(E_F)$ and $-\frac{N'(E_F)}{N(E_F)}$ is expected to be larger than for the doping of 1.46 electrons per supercell. However, this is not the case for the corresponding S_{DFT} [blue curve, Fig. 11(a)], which is slightly reduced in height and also narrowed: at elevated temperatures,

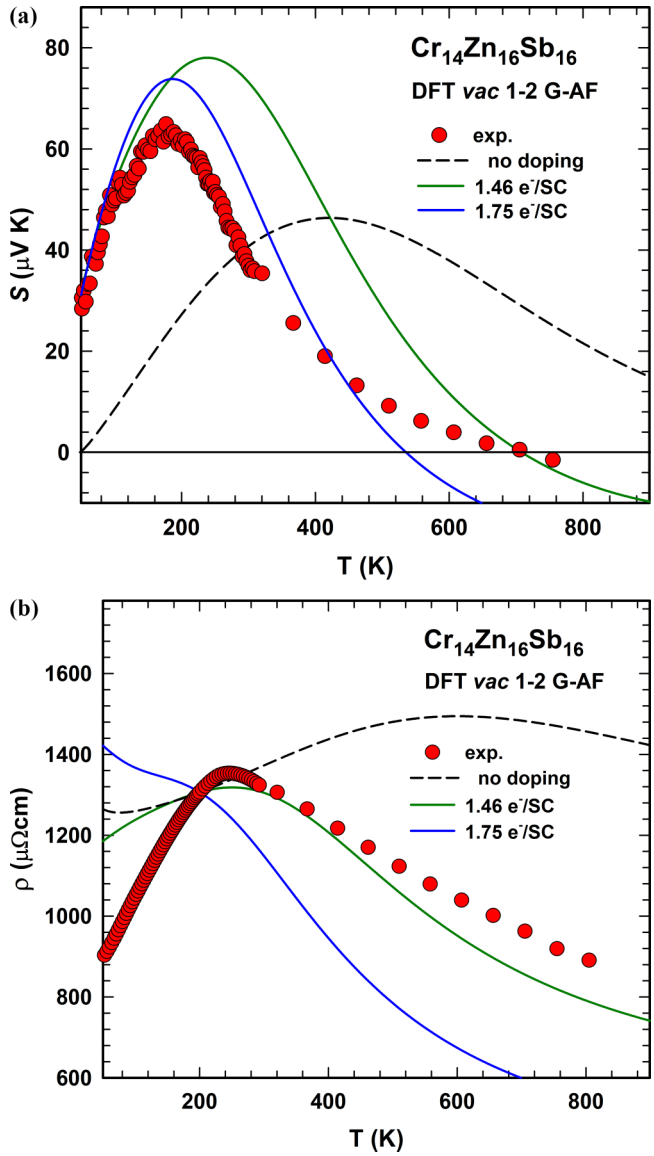

FIG. 11. Measured and DFT-calculated Seebeck coefficient and resistivity as a function of temperature for the *vac*1-2 G-AF structure of $Cr_{14}Zn_{16}Sb_{16}$. Measurements done for the sample $Cr_{0.86}ZnSb$. (a) Isotropic Seebeck coefficient S. DFT data for undoped case and two charge doping levels of $-1.46\,e^-$/supercell and $-1.75\,e^-$/supercell. (b) Isotropic resistivity ρ. DFT data for undoped case and two charge doping levels of $1.46\,e^-$/supercell. and $1.75\,e^-$/supercell. The relaxation time τ was determined according to $\rho_{\mathrm{DFT}}\,(200\,\mathrm{K}) = \rho_{\mathrm{expt}}\,(200\,\mathrm{K})$.

electronic states close to or above the pseudogap gain more influence.

The crossing with the zero line is now at 536 K. Comparing just the two doped DFT Seebeck coefficients with measurement does not clearly indicate which one is better. However, the situation changes when resistivity results are considered.

Figure 11(b) clearly shows a peaked behavior of the measured resistivity ρ_{expt}. A maximum of 1354 μΩ cm is reached at 240 K; subsequently $\rho_{\mathrm{expt}}(T)$ decreases with rising temperatures down to 890 μΩ cm at 806 K. As mentioned above, because of the unknown constant relaxation τ the DFT data for ρ are fitted to the measurement at 200 K. Therefore, all curves cross at this temperature. The DFT resistivity for the undoped case is very different from ρ_{expt}, because it increases above 200 K up to a shallow maximum at 600 K. For the two doping levels, however, the DFT results change strikingly, showing also a decreasing ρ with T larger than 220 K. The decrease is most dramatic for the doping of 1.75 electrons, making the agreement with experiment rather poor.

However, for the doping of 1.46 electrons, the DFT ρ above 220 K is just slightly smaller than measurement. A perfect agreement cannot be expected, because the ρ_{DFT} does not include any effects of electron-phonon scattering; it is purely based on the band velocities of the electronic states. It is expected that at elevated temperatures electron-phonon scattering broadens the purely electronic $\rho_{\mathrm{DFT}}(T)$ to a certain degree. Electron-phonon scattering is also neglected for $S_{\mathrm{DFT}}(T)$. Presumably, the effects will cancel out to some extent, because of the fraction in Eq. (2).

The mentioned doping levels are chosen with respect to the large supercell of composition $Cr_{14}Zn_{16}Sb_{16}$. By doping, deviations of the stoichiometry of the measured sample from the ideal composition of the supercell are modeled assuming that – apart from shifting E_{F} – the DFT electronic structure remains unchanged otherwise. With respect to the composition $Cr_{0.86}ZnSb$, the chosen doping amounts have to be divided by 16 assuming Zn or Sb are in excess, resulting in a stoichiometry of $Zn_{1.1}$ or $Sb_{1.1}$, its deviation from 1 being hardly measurable.

Discussing DFT ρ below $T = 200$ K one observes three significantly different behaviors for the three different doping levels, with $\rho(1.46\,e^-/\mathrm{SC})$ as the most reasonable one; however, one should be careful about the interpretation of DFT ρ and S at very low temperatures. The reason is that the derivative of the Fermi-Dirac function $\frac{\partial f^{\mathrm{FD}}}{\partial E(\vec{k})}$ is getting very narrow at very low temperatures. Therefore, for sampling a sufficiently large number of electronic states, the number of $\vec{k}$ points in the Brillouin zone must be very large. This can be done but it needs an extensive and time-consuming study, which is beyond the scope of our paper.

VI. CONCLUSION

Our comprehensive study of the $Cr_{0.86}ZnSb$ system through both experimental analysis and theoretical simulations has elucidated the unique properties of this compound arising from Cr vacancies. A detailed investigation of the $Cr_{1-x}ZnSb$ phase space yielded only $Cr_{0.86}ZnSb$ as a stable, phase-pure compound, which crystallizes in the MnAlGe-type structure with Cr vacancies. The experimental results obtained from magnetization and specific heat measurements reveal antiferromagnetic behavior with a Néel temperature of 220 K. In order to complement macroscopic bulk measurements with a local probe technique suited to reveal the approximate magnetically ordered volume fraction, muon spin relaxation measurements were conducted and the obtained temperature-dependent zero-field relaxation data unambiguously confirm an intrinsic magnetic phase transition of $Cr_{0.86}ZnSb$ at around 220 K. Regarding the transport properties, measurements over a wide temperature range from 4 to 800 K were performed.

Both resistivity and Seebeck coefficients were found to exhibit distinct positive maxima in their temperature-dependent behavior. At about the same temperature, the inverse of the Hall coefficient exhibits a distinct upturn.

From analyzing the experimental data, the electronic structure was determined as a narrow-gap semimetal with a small pseudogap in the vicinity of the Fermi energy. Subsequently, DFT calculations for virtual $Cr_2Zn_2Sb_2$ as well as for vacancy structures were conducted, using a supercell of composition $Cr_{14}Zn_{16}Sb_{16}$ to ensure perfect antiferromagnetic ordering. DFT confirms that the Cr-vacancy structure is energetically more stable than the stoichiometric compound. Moreover, the analysis of formation energies regarding different spin configurations reveals $Cr_{0.875}ZnSb$ to be antiferromagnetic, in line with experimental results. The calculations reveal large site-projected local magnetic moments of Cr of 2 μ_B − 2.6 μ_B screened by delocalized *p* states of Sb. The Cr-vacancy defect structure with vacancies along the *c* axis reveals a unique pseudogap in the DOS which drops down steeply at two electrons above the Fermi energy. Such a feature is of importance for calculating suitable transport properties. By application of the BOLTZTRAP code [31], Seebeck coefficients and electronic resistivities are calculated directly from the DFT electronic structure, and excellent agreement with the measured data is achieved, when suitable doping is applied. The electronic structure of additional defects, such as placing Zn on a Cr-vacancy site and substituting one Zn atom by Sb also shows the hallmark of the pseudogap.

Our research highlights the significance of structural defects in $Cr_{0.86}ZnSb$ and formal consideration of vacancies and their configuration when analyzing such compounds. By combining theoretical methods with careful analysis of experimental data, we comprehensively characterized the magnetic and electronic structure, revealing the vacancy-driven formation of a pseudogap close to the Fermi energy in the antiferromagnetic $Cr_{0.86}ZnSb$.

The raw data from the local probe μSR studies are accessible through the ISIS Neutron and Muon Source Data Journal [64].

ACKNOWLEDGMENTS

This research was supported by MEYS, the Czech Republic, via the bilateral mobility project 8J23AT014 co-sponsored by the Austrian WTZ-CZ08/2023 and by JST, project MIRAI No. JPMJMI19A1. A part of this research was carried out at the EMU μSR beam line of the ISIS facility at the Rutherford Appleton Laboratory, United Kingdom. Beamtime was allocated via the Xpress proposal XB2291031.

[1] J. M. Mena and T. Gruhn, Search of stable structures in cation deficient (V, Nb) CoSb half-Heusler alloys by an atomic cluster expansion, J. Mater. Chem. A **9**, 21111 (2021).

[2] Z. Zhu, Y. Cheng, and U. Schwingenschlögl, Vacancy induced half-metallicity in half-Heusler semiconductors, Phys. Rev. B **84**, 113201 (2011).

[3] N. Roth, T. Zhu, and B. B. Iversen, A simple model for vacancy order and disorder in defective half-Heusler systems, IUCrJ **7**, 673 (2020).

[4] F. Luo, J. Wang, C. Zhu, X. He, S. Zhang, J. Wang, H. Liu, and Z. Sun, 18-electron half-Heusler compound $Ti_{0.75}NiSb$ with intrinsic Ti vacancies as a promising thermoelectric material, J. Mater. Chem. A **10**, 9655 (2022).

[5] K. Xia, Y. Liu, S. Anand, G. J. Snyder, J. Xin, J. Yu, X. Zhao, and T. Zhu, Enhanced thermoelectric performance in 18-electron $Nb_{0.8}CoSb$ half-Heusler compound with intrinsic Nb vacancies, Adv. Funct. Mater. **28**, 1705845 (2018).

[6] L. Huang, T. Liu, A. Huang, G. Yuan, J. Wang, J. Liao, X. Lei, Q. Zhang, and Z. Ren, Enhanced thermoelectric performance of nominal 19-electron half-Heusler compound NbCoSb with intrinsic Nb and Sb vacancies, Mater. Today Phys. **20**, 100450 (2021).

[7] K. Xia, C. Hu, C. Fu, X. Zhao, and T. Zhu, Half-Heusler thermoelectric materials, Appl. Phys. Lett. **118**, 140503 (2021).

[8] S. Tan, P. Nan, K. Xia, H. Yang, T. Zhu, B. Ge, and W. Zhang, Sublattice short-range order and modified electronic structure in defective half-Heusler $Nb_{0.8}CoSb$, J. Phys. Chem. C **125**, 1125 (2020).

[9] Y. Kimura, T. Tanoguchi, Y. Sakai, Y. W. Chai, and Y. Mishima, Effect of vacancy-site occupation in half-Heusler compound ZrNiSn on phase stability and thermoelectric properties, MRS Online Proc. Libr. **1295**, 335 (2011).

[10] W. Ren, W. Xue, S. Guo, R. He, L. Deng, S. Song, A. Sotnikov, K. Nielsch, J. van den Brink, G. Gao, and S. Chen, Vacancy-mediated anomalous phononic and electronic transport in defective half-Heusler ZrNiBi, Nat. Commun. **14**, 4722 (2023).

[11] I. S. Elfimov, S. Yunoki, and G. A. Sawatzky, Possible path to a new class of ferromagnetic and half-metallic ferromagnetic materials, Phys. Rev. Lett. **89**, 216403 (2002).

[12] F. G. Aliev, V. V. Moshchalkov, V. V. Kozyrkov, M. K. Zalyalyutdinov, V. U. Pryadun, and R. V. Skolozdra, Transport and magnetic properties of intermetallic systems RNiM (R = U, Ce, Er, Ho, Tm, Yb, Sc, Ti, Zr, Hf; M = Sn, Sb), J. Magn. Magn. Mater. **76**, 295 (1988).

[13] K. Kirievsky, M. Shlimovich, D. Fuks, and Y. Gelbstein, An ab-initio study of the thermoelectric enhancement potential in nano-grained TiNiSn, Phys. Chem. Chem. Phys. **16**, 20023 (2014).

[14] G. Schierning, R. Chavez, R. Schmechel, B. Balke, G. Rogl, and P. Rogl, Concepts for medium-high to high temperature thermoelectric heat-to-electricity conversion: A review of selected materials and basic considerations of module design, Transl. Mater. Res. **2**, 025001 (2015).

[15] S. Sakurada and N. Shutoh, Effect of Ti substitution on the thermoelectric properties of (Zr,Hf)NiSn half Heusler compounds, Appl. Phys. Lett. **86**, 082105 (2005).

[16] G. Rogl, P. Sauerschnig, Z. Rykavets, V. V. Romaka, P. Heinrich, B. Hinterleitner, A. Grytsiv, E. Bauer, and P. Rogl, (V,Nb)-doped half Heusler alloys based on {Ti,Zr,Hf}NiSn with high ZT, Acta Mater. **131**, 336 (2017).

[17] I. Chumak, V. Pavlyuk, G. Dmytriv, and J. Stępień-Damm, Phase equilibria and crystal structure of compounds in the Fe-Zn-Sb system at 570 K, J. Alloys Compd. **307**, 223 (2000).

[18] Z. Zhu, X. Su, J. Wang, C. Wu, and Y. Wu, Experimental investigation and thermodynamic calculation of the Zn-Fe-Sb system, CALPHAD: Comput. Coupling Phase Diagrams Thermochem. **34**, 98 (2010).

[19] I. Chumak and V. Pavlyuk, Interaction of the components in the Ni-Zn-Sb ternary system at 570 K, J. Alloys Compd. **367**, 85 (2004).

[20] D.-B. Xiong, N. L. Okamoto, T. Waki, Y. Zhao, K. Kishida, and H. Inui, High$-T_C$ ferromagnetic semiconductor-like behavior and unusual electrical properties in compounds with a $2 \times 2 \times 2$ superstructure of the half-Heusler phase, Chem. - Eur. J. **18**, 2536 (2012).

[21] E. A. Bensen, K. Ciesielski, L. C. Gomes, B. R. Ortiz, J. Falke, O. Pavlosiuk, D. Weber, T. L. Braden, K. X. Steirer, D. Szymański, J. E. Goldberger, C.-Y. Kuo, C.-T. Chen, C.-F. Chang, L. H. Tjeng, D. Kaczorowski, E. Ertekin, and E. S. Toberer, Anomalous electronic properties in layered, disordered ZnVSb, Phys. Rev. Mater. **5**, 015002 (2021).

[22] K. Ciesielski, L. C. Gomes, G. A. Rome, E. A. Bensen, J. M. Adamczyk, D. Kaczorowski, E. Ertekin, and E. S. Toberer, Phys. Rev. Mater. **6**, 063602 (2022), see also the Supplemental Material [49].

[23] J. Rodriguez-Carvajal, Recent advances in magnetic structure determination by neutron diffraction, Physica B **192**, 55 (1993).

[24] W. Wacha, An integrated software system for x-ray structure analysis, Diploma thesis, TU Wien, Austria, 1989.

[25] Bruker advanced x-ray solutions, APEX2 User Manual, Version 1.22 (Bruker AXS Inc., 2004). For APEXII, SAINT, and SADABS see Bruker Analytical X-ray Instruments, Inc., Madison, WI (2008).

[26] INCA Energy-300 and INCA Wave 700, Oxford Instruments Analytical Ltd., United Kingdom (2000).

[27] R. Resel, E. Gratz, A. T. Burkov,T. Nakama, M. Higa, and K. Yagasaki, Thermopower measurements in magnetic fields up to 17 tesla using the toggled heating method, Rev. Sci. Instrum. **67**, 1970 (1996).

[28] S. R. Giblin, S. P. Cottrell, P. J. C. King, S. Tomlinson, S. J. S. Jago, L. J. Randall, M. J. Roberts, J. Norris, S. Howarth, Q. B. Mutamba, N. J. Rhodes, and F. A. Akeroyd, Optimising a muon spectrometer for measurements at the ISIS pulsed muon source, Nucl. Instrum. Methods Phys. Res. A **751**, 70 (2014).

[29] F. L. Pratt, WIMDA: A muon data analysis program for the Windows PC, Physica B **289–290**, 710 (2000).

[30] G. Kresse and J. Furthmüller, Efficiency of *ab initio* total energy calculations for metals and semiconductors using a plane-wave basis set, Comput. Mater. Sci. **6**, 15 (1996).

[31] G. Kresse and J. Furthmüller, Efficient iterative schemes for *ab initio* total energy calculations using a plane-wave basis set, Phys. Rev. B **54**, 11169 (1996).

[32] P. Blöchl, Projector augmented-wave method, Phys. Rev. B **50**, 17953 (1994).

[33] G. Kresse and D. Joubert, From ultrasoft pseudopotentials to the projector augmented-wave method, Phys. Rev. B **59**, 1758 (1999).

[34] J. P. Perdew, K. Burke, and M. Ernzerhof, Generalized gradient approximation made simple, Phys. Rev. Lett. **77**, 3865 (1996).

[35] S. L. Dudarev, G. A. Botton, S. Y. Savrasov, C. J. Humphreys, and A. P. Sutton, Electron-energy-loss spectra and the structural stability of nickel oxide: An LSDA+U study, Phys. Rev. B **57**, 1505 (1998).

[36] R. Bader, *Atoms in Molecules: A Quantum Theory* (Oxford University Press, New York, 1994).

[37] R. Bader, in *The Encyclopedia of Computational Chemistry*, edited by P. v. R. Schleyer (Wiley, Chichester, 1998), Vol. 1, p. 6486.

[38] G. Henkelman, A. Arnaldsson, and H. Jonsson, A fast and robust algorithm for Bader decomposition of charge density, Comput. Mater. Sci. **36**, 354 (2006).

[39] E. Sanville, S. D. Kenny, R. Smith, and G. Henkelman, Improved grid-based algorithm for Bader charge allocation, J. Comput. Chem. **28**, 899 (2007).

[40] W. Tang, E. Sanville, and G. Henkelman, A grid-based Bader analysis algorithm without lattice bias, J. Phys.: Condens. Matter **21**, 084204 (2011).

[41] M. Yu, and D. R. Trinkle, Accurate and efficient algorithm for Bader charge integration, J. Chem. Phys. **134**, 064111 (2011).

[42] G. K. Madsen and D. J. Singh, BoltzTrap: A code for calculating band-structure dependent quantities, Comput. Phys. Commun. **175**, 67 (2006).

[43] P. Villars and K. Cenzual, Pearson's Crystal Data: Crystal Structure Database for Inorganic Compounds, Release 2021/22. ASM International, Materials Park, OH.

[44] G. M. Sheldrick, SHELX—Program for crystal structure refinement, Acta Crystallogr. A **64**, 112 (2008); Windows version OSCAIL by P. McArdle, K. Gilligan, D. Cunningham, R. Dark, and M. Mahon, Cryst. Eng. Comm. **6**, 303 (2004).

[45] E. Parthé, L. Gelato, B. Chabot, M. Penzo, K. Censual, and R. Gladyshevskii, TYPIX—Standardized Data and Crystal Chemical Characterization of Inorganic Structure Types (Springer-Verlag, Berlin, 1994); J. Appl. Crystallogr. **20**, 139 (1987).

[46] W. B. Pearson, *The Crystal Chemistry and Physics of Metals and Alloys* (Wiley-Interscience, New York, 1972); The 12-coordinated metallic radii in Table 4-4 of this book have been taken from E. Teatum, K. Gschneidner, and J. Waber, *Report LA-2345* (U.S. Department of Commerce, Washington, DC, 1960).

[47] P. A. Stadelmann, Java Electron Microscopy Software, https://www.jems-swiss.ch (2024).

[48] P. A. Stadelmann, EMS—a software package for electron diffraction analysis and HREM image simulation in materials science, Ultramicroscopy **21**, 131 (1987).

[49] See Supplemental Material at http://link.aps.org/supplemental/10.1103/PhysRevB.110.195124 for additional density-functional theory calculation results and the magnetic field dependence of $\rho(T)$. The Supplemental Material includes additional references [60–63].

[50] K. Momma and F. Izumi, VESTA 3 for three-dimensional visualization of crystal, volumetric and morphology data, J. Appl. Crystallogr. **44**, 1272 (2011).

[51] R. Hafner, D. Spisak, R. Lorenz, and J. Hafner, Magnetic ground state of Cr in density-functional theory, Phys. Rev. B **65**, 184432 (2002).

[52] E. Fawcett, H. Alberts, V. Galkin, and D. N. J. Yakhmi, Spin-density-wave antiferromagnetism in chromium alloys, Rev. Mod. Phys. **66**, 25 (1994).

[53] P. Marcus, S.-L. Qiu, and V. Moruzzi, The mechanism of antiferromagnetism in chromium, J. Phys.: Condens. Matter **10**, 6541 (1998).

[54] F. Garmroudi, M. Parzer, A. Riss, A. Pustogow, T. Mori, and E. Bauer, Pivotal role of carrier scattering for semiconductorlike transport in Fe_2VAl, Phys. Rev. B **107**, L081108 (2023).

[55] A. F. May and G. J. Snyder, Introduction to modeling thermoelectric transport at high temperatures, in *Materials, Preparation, and Characterization in Thermoelectrics*, edited by D. M. Rowe (CRC Press, Boca Raton, FL, 2012).

[56] F. Garmroudi, A. Riss, M. Parzer, N. Reumann, H. Müller, E. Bauer, S. Khmelevskyi, R. Podloucky, T. Mori, K. Tobita, Y. Katsura, and K. Kimura, Boosting the thermoelectric performance of Fe_2VAl-type Heusler compounds by band engineering, Phys. Rev. B **103**, 085202 (2021).

[57] B. Hinterleitner, F. Garmroudi, N. Reumann, T. Mori, E. Bauer, and R. Podloucky, The electronic pseudo band gap states and electronic transport of the full-Heusler compound Fe 2 VAl, J. Mater. Chem. C **9**, 2073 (2021).

[58] F. Garmroudi, M. Parzer, A. Riss, S. Beyer, S. Khmelevskyi, T. Mori, M. Reticcioli, and E. Bauer, Large thermoelectric power factors by opening the band gap in semimetallic Heusler alloys, Mater. Today Phys. **27**, 100742 (2022).

[59] G. Rogl, F. Garmroudi, A. Riss, X. Yan, J. G. Sereni, E. Bauer, and P. Rogl, Understanding thermal and electronic transport in high-performance thermoelectric skutterudites, Intermet. **146**, 107567 (2022).

[60] A. Sommerfeld, Zur Elektronentheorie der Metalle auf Grund der Fermischen Statistik: I. Teil: Allgemeines, Strömungs-und Austrittsvorgänge, Z. Phys. **47**, 1 (1928).

[61] W. F. Brinkman and S. Engelsberg, Spin-fluctuation contributions to the specific heat, Phys. Rev. **169**, 417 (1968).

[62] H. Michor, M. El-Hagary, M. Della Mea, M. W. Pieper, M. Reissner, G. Hilscher, S Khmelevskyi, P. Mohn, G. Schneider, G. Giester, and P. F. Rogl, Itinerant electron metamagnetism in $LaCo_9Si_4$, Phys. Rev. B **69**, 081404(R) (2004).

[63] H. Michor, M. El-Hagary, S. Özcan, A. Horyn, E. Bauer, M. Reissner, G. Hilscher, S. Khmelevskyi, P. Mohn, and P. Rogl, Weak itinerant ferromagnetism in YCo_9Si_4, Physica B **359–361**, 1177 (2005).

[64] H. Michor and S. Cottrell, "Local probe μSR studies of the magnetic ground state of CrZnSb", STFC ISIS Neutron and Muon Source (2024), https://doi.org/10.5286/ISIS.E/ISIS.E.RB2291031-2.